

Fluorescence near metal tips: The roles of energy transfer and surface plasmon polaritons

Nader A. Issa* and Reinhard Guckenberger

Max Planck Institute of Biochemistry, Dept. of Molecular Structural Biology
Am Klopferspitz 18, D-82152 Martinsried, Germany

*Corresponding author: issa@biochem.mpg.de

Abstract: We simulate the remarkable changes that occur to the decay rates of a fluorescent molecule as a conical metal tip approaches. A new and simple model is developed to reveal and quantify which decay channels are responsible. Our analysis, which is independent of the method of molecular excitation, shows some universal characteristics. As the tip-apex enters the molecule's near-field, the creation of surface plasmon polaritons can become extraordinarily efficient, leading to an increase in the nonradiative rate and, by proportional radiative-damping, in the radiative rate. Enhancements reaching 3 orders of magnitude have been found, which can improve the apparent brightness of a molecule. At distances less than ~5nm, short-ranged energy transfer to the nano-scale apex quickly becomes dominant and is entirely nonradiative.

©2007 Optical Society of America

OCIS codes: (240.0240) Optics at surfaces; (240.6680) Surface plasmons; (180.5810) Scanning microscopy; (170.2520) Fluorescence microscopy; (260.2510) Fluorescence; (260.3910) Metals, optics of.

References and links

1. R. R. Chance, A. Prock, and R. Silbey, "Molecular fluorescence and energy transfer near interfaces," *Adv. Chem. Phys.* 37, 1-65 (1978).
2. G. W. Ford, and W. H. Weber, "Electromagnetic-interactions of molecules with metal-surfaces," *Phys. Rep.* 113, 195-287 (1984).
3. W. L. Barnes, "Fluorescence near interfaces: the role of photonic mode density," *J. Mod. Opt.* 45, 661-699 (1998).
4. R. X. Bian, R. C. Dunn, and X. S. Xie, "Single molecule emission characteristics in near-field microscopy," *Phys. Rev. Lett.* 75, 4772-4775 (1995).
5. N. Hayazawa, Y. Inouye, and S. Kawata, "Evanescent field excitation and measurement of dye fluorescence in a metallic probe near-field scanning optical microscope," *J. Microsc.* 194, 472-476 (1999).
6. E. J. Sanchez, L. Novotny, and X. S. Xie, "Near-field fluorescence microscopy based on two-photon excitation with metal tips," *Phys. Rev. Lett.* 82, 4014-4017 (1999).
7. T. J. Yang, G. A. Lessard, and S. R. Quake, "An apertureless near-field microscope for fluorescence imaging," *App. Phys. Lett.* 76, 378-380 (2000).
8. A. Kramer, W. Trapesinger, B. Hecht, and U. P. Wild, "Optical near-field enhancement at a metal tip probed by a single fluorophore," *App. Phys. Lett.* 80, 1652-1654 (2002).
9. H. G. Frey, S. Witt, K. Felderer, and R. Guckenberger, "High-resolution imaging of single fluorescent molecules with the optical near-field of a metal tip," *Phys. Rev. Lett.* 93, 200801 (2004).
10. J. N. Farahani, D. W. Pohl, H. J. Eisler, and B. Hecht, "Single quantum dot coupled to a scanning optical antenna: A tunable superemitter," *Phys. Rev. Lett.* 95 (2005).
11. F. M. Huang, F. Festy, and D. Richards, "Tip-enhanced fluorescence imaging of quantum dots," *App. Phys. Lett.* 87 (2005).
12. H. Gersen, M. F. Garcia-Parajo, L. Novotny, J. A. Veerman, L. Kuipers, and N. F. Van Hulst, "Near-field effects in single molecule emission," *J. Microsc.* 202, 374-378 (2001).
13. P. Anger, P. Bharadwaj, and L. Novotny, "Enhancement and quenching of single-molecule fluorescence," *Phys. Rev. Lett.* 96, 4 (2006).
14. S. Kuhn, U. Hakanson, L. Rogobete, and V. Sandoghdar, "Enhancement of single-molecule fluorescence using a gold nanoparticle as an optical nanoantenna," *Phys. Rev. Lett.* 97 (2006).
15. F. Cannone, G. Chirico, A. R. Bizzarri, and S. Cannistraro, "Quenching and blinking of fluorescence of a single dye molecule bound to gold nanoparticles," *J. Phys. Chem. B* 110, 16491-16498 (2006).

16. F. D. Stefani, K. Vasilev, N. Bocchio, F. Gaul, A. Pomozzi, and M. Kreiter, "Photonic mode density effects on single-molecule fluorescence blinking," *New J. Phys.* 9 (2007).
17. F. D. Stefani, K. Vasilev, N. Bocchio, N. Stoyanova, and M. Kreiter, "Surface-plasmon-mediated single-molecule fluorescence through a thin metallic film," *Phys. Rev. Lett.* 94 (2005).
18. J. R. Lakowicz, "Plasmonics in biology and plasmon-controlled fluorescence," *Plasmonics* 1, 5-33 (2006).
19. Y. X. Zhang, K. Aslan, M. J. R. Previte, and C. D. Geddes, "Metal-enhanced fluorescence: Surface plasmons can radiate a fluorophore's structured emission," *App. Phys. Lett.* 90 (2007).
20. G. Winter, and W. L. Barnes, "Emission of light through thin silver films via near-field coupling to surface plasmon polaritons," *App. Phys. Lett.* 88 (2006).
21. M. Thomas, J. J. Greffet, R. Carminati, and J. R. Arias-Gonzalez, "Single-molecule spontaneous emission close to absorbing nanostructures," *App. Phys. Lett.* 85, 3863-3865 (2004).
22. J. T. Krug II, E. J. Sanchez, and X. S. Xie, "Fluorescence quenching in tip-enhanced nonlinear optical microscopy," *App. Phys. Lett.* 86 (2005).
23. F. M. Huang, and D. Richards, "Fluorescence enhancement and energy transfer in apertureless scanning near-field optical microscopy," *J. Opt. A*, 8, S234-S238 (2006).
24. C. Girard, O. J. F. Martin, and A. Dereux, "Molecular lifetime changes induced by nanometer-scale optical-fields," *Phys. Rev. Lett.* 75, 3098-3101 (1995).
25. L. Novotny, "Single molecule fluorescence in inhomogeneous environments," *App. Phys. Lett.* 69, 3806-3808 (1996).
26. A. Rahmani, P. C. Chaumet, and F. de Fornel, "Environment-induced modification of spontaneous emission: Single-molecule near-field probe," *Phys. Rev. A* 6302 (2001).
27. A. Downes, D. Salter, and A. Elfick, "Finite element simulations of tip-enhanced Raman and fluorescence spectroscopy," *J. Phys. Chem. B* 110, 6692-6698 (2006).
28. N. A. Issa, and R. Guckenberger, "Optical nanofocusing on tapered metallic waveguides," *Plasmonics* 2, 31-37 (2007).
29. P. M. Whitmore, H. J. Robota, and C. B. Harris, "Mechanisms for electronic-energy transfer between molecules and metal-surfaces - a comparison of silver and nickel," *J. Chem. Phys.* 77, 1560-1568 (1982).
30. P. Avouris, and B. N. J. Persson, "Excited-states at metal-surfaces and their nonradiative relaxation," *J. Phys. Chem.* 88, 837-848 (1984).
31. P. B. Johnson, and R. W. Chirsty, "Optical constants of the noble metals," *Phys. Rev. B* 6, 4370-4379 (1972).
32. D. R. Lide, ed. *CRC handbook of chemistry and physics* (CRC press, London, 1996).
33. J. Takahara, S. Yamagishi, H. Taki, A. Morimoto, and T. Kobayashi, "Guiding of a one-dimensional optical beam with nanometer diameter," *Opt. Lett.* 22, 475-477 (1997).
34. E. Dulkeith, M. Ringler, T. A. Klar, J. Feldmann, A. M. Javier, and W. J. Parak, "Gold nanoparticles quench fluorescence by phase induced radiative rate suppression," *Nano Lett.* 5, 585-589 (2005).
35. R. Carminati, J. J. Greffet, C. Henkel, and J. M. Vigoureux, "Radiative and non-radiative decay of a single molecule close to a metallic nanoparticle," *Opt. Commun.* 261, 368-375 (2006).
36. L. Novotny, and C. Hafner, "Light propagation in a cylindrical waveguide with a complex, metallic, dielectric function," *Phys. Rev. E* 50, 4094-4106 (1994).
37. A. W. Snyder, and J. D. Love, *Optical waveguide theory* (Chapman and Hall, New York, 1983).

1. Introduction

A surface nearby to a fluorescent molecule in its excited state can dramatically influence the rates of its decay transitions [1-3]. The interface can provide additional nonradiative decay channels, as well as alter the rate of radiative decay and its spatial distribution. It is now widely appreciated that metallic nano-particles and scanning probes [4-14] can either quench fluorescence or beneficially enhance fluorescence, leading to brighter fluorescent molecules and improved stability [15, 16]. It has become clear that there exist enormous potential benefits of fluorescence engineering to technologies, such as fluorescence imaging and biochemical identification. In this paper we enquire about an arrangement akin to that used in aperture-less Scanning Near-field Optical Microscopy (SNOM). We study the decay of an excited molecule, independently of the illumination scheme. Despite the widespread use of this microscopy, much is still unknown about the influence of the metal tip on fluorescence. In response, we simulate this system to reveal some of the physics of interaction between an excited molecule and a conical, infinitely long metal tip with nano-scale apex. The dramatic fluorescence-lifetime changes we observe can be exploited to great effect.

The important influence of Surface Plasmon Polaritons (SPPs) (both local and propagating) on fluorescence is increasingly being emphasized in current literature [17-20]. Alterations to both radiative and nonradiative decay rates have been attributed to SPPs.

However, to be quantitative about the role of SPPs in most systems has been very difficult in experiment and theory. The exceptions are typically simple arrangements that permit analytic solutions [3, 17, 20]. Simulations of fluorescence lifetimes in SNOM have explored fluorescence spectra [14, 21], tip-molecule distance dependence [13, 22, 23] and imaging contrast [24-27]. These studies generally assume a truncated metal tip, which can lead to significant deviations from results obtained with real, elongated SNOM tips. We present here a much more realistic analogue. Most significantly, we present the first quantification of SPPs excited on the tip by near-fields of the molecule, which we find to be both radiative and nonradiative. We also identify a rate of purely nonradiative energy transfer to the nano-apex of the tip. The influence on the apparent quantum efficiency, radiative and nonradiative decay rates are explored in depth. In addition to elucidating some underlying physics, our numerical results provide a reference for effective SNOM design, where molecule excitation can be achieved by single or multi-photon excitation, conventional far-field methods, or other recent methods employing nanofocusing SPP modes [28].

2. Background theory

In this paper we use a phenomenological classical oscillating electric dipole \mathbf{p} to represent our emitter, a two-level molecule. The magnitude of the electric dipole is unchanged by its environment. This theoretical treatment has consistently proven to be an excellent approximation [1-3]. The total decay rate γ is commonly measured experimentally by the inverse of the excited-state lifetime, and is given by $\gamma = P/(\hbar\omega)$, where P is the total rate of energy dissipation and ω is the angular frequency (vacuum wavelength λ). The total decay rate is proportional to the partial Local Density Of States (LDOS). It can be separated as

$$\gamma = \gamma_r + \gamma_i + \gamma_{nr}. \quad (1)$$

γ_r is the radiative decay rate, accounting for electromagnetic power in the far-field, i.e. photons. γ_i is the decay rate intrinsic to the molecule and is associated with a nonradiative, intra-molecular energy dissipation. An additional nonradiative rate γ_{nr} accounts for other forms of electromagnetic energy dissipation in the molecule's surrounding. With a metal tip nearby it describes processes of thermal dissipation, mediated primarily by the creation of electron-hole pairs (excitons), such as dissipated SPPs. Classically, one can picture this dissipation as the resistive heating of the metal by lossy conduction currents $\mathbf{j} = \omega \text{Im}(\epsilon_{\text{metal}}) \epsilon_0 \mathbf{E}$ induced by the dipole field \mathbf{E} , where the proportionality constant (conductivity) is related to the relative dielectric constant of the metal ϵ_{metal} . The nonradiative rate for an *infinitely long tip* is then

$$\gamma_{nr} = \frac{1}{\hbar\omega} \int_{\text{tip}} \frac{1}{2} \text{Re}(\mathbf{j}^* \cdot \mathbf{E}) dV. \quad (2)$$

We argue that the system considered here permits us to further separate the nonradiative rate into two meaningful contributions:

$$\gamma_{nr} = \gamma_{\text{SPP}} + \gamma_{\text{LET}}. \quad (3)$$

γ_{SPP} is the *nonradiative-SPP* rate, i.e. the rate at which SPPs excited by the molecule are thermally dissipated in an *infinite* tip. Since SPPs can propagate for distances over a few microns on the tip, this is a longer-ranged dissipation. γ_{LET} is the rate of nonradiative energy transfer to the nano-apex of the tip. This shorter-ranged dissipation is referred to as local energy transfer (LET). The definitions and validations for both these terms are provided in Section 5. Such a separation has been previously proposed for flat interfaces [2, 3, 29], but to our knowledge has never been applied to non-planar geometries.

The rate of electromagnetic energy dissipation P_{EM} is calculated in our simulations by either integrating the Poynting vector over a surface enclosing the molecule, or equivalently by the expression $P_{\text{EM}} = \omega \text{Im}[\mathbf{p}^* \cdot \mathbf{E}(\mathbf{r}_o)]/2$, where $\mathbf{E}(\mathbf{r}_o)$ is the molecule's emission field at

precisely the position \mathbf{r}_o of the molecule [25]. It allows us to calculate the radiative decay rate by: $\gamma_r = P_{EM}/(\hbar\omega) - \gamma_{nr}$.

The radiative decay rate in the absence of the tip γ_o will depend on the surrounding medium and substrate nearby. If the medium and substrate are lossless, we define the initial quantum efficiency as $q_o = \gamma_o/(\gamma_o + \gamma_r)$. With the tip nearby, we define the *apparent* quantum efficiency and express it as a function of the initial quantum efficiency:

$$q = \frac{\gamma_r}{\gamma} = \frac{\gamma_r}{\gamma_r + \gamma_{nr} + (1/q_o - 1)\gamma_o}. \quad (4)$$

A reduction in q is commonly referred to as apparent quenching of fluorescence. A table of most relevant terms used in this paper is provided in Appendix B for convenience.

2.1. Excitation and detection

It is the photon detection rate γ_{det} that is most directly measured experimentally, and which can be inferred from the results we present. For a single molecule it is given by $\gamma_{det} = \xi N \gamma_r$, where ξ is the overall detection efficiency of the instrument and N is the probability of finding the molecule in its excited state. In the absence of a triplet bottle-neck, it is instructive to consider two extremes of excitation intensity. Near saturation $N \approx 1$ and the detection rate is proportional to the radiative decay rate. More commonly, excitation is far below saturation, where $\gamma_{det} = \xi \gamma_{exc} q$. In this case the excitation rate γ_{exc} plays a role together with the apparent quantum efficiency. We leave the system of excitation to the reader. Furthermore, we have not considered the very important role of near-field excitation enhancement in this paper. Rather we will only outline that $\gamma_{exc} \propto |\mathbf{n} \cdot \mathbf{E}_{exc}|^2$, where \mathbf{n} is the unit vector in the direction of the molecule's *absorption* dipole moment and \mathbf{E}_{exc} is the excitation electric field (at arbitrary wavelength), comprising the incident field and near-field of the tip.

The rate for radiation directed into the lower half space is γ_r^\downarrow . The ratio $\gamma_r^\downarrow/\gamma_r$ can be used as an indicator of the change in the emission distribution, caused by the tip above the molecule. It is also an important factor in the overall detection efficiency ξ of most common instruments. The natural emission from a molecule on a glass substrate (oriented perpendicularly to the surface) gives $\gamma_r^\downarrow/\gamma_r \approx 85\%$, determined from the analytic solution [1].

2.2. Limitations of the model

For molecule-tip separations much less than 10nm, the approximations in our 'classical' model are addressed in the modern review by Barnes [3]. The model notably excludes effects of non-locality and electron scattering at the interface. It is known that the model may underestimate nonradiative rates for distances in the range from 0.5nm to 10nm, typically only at infrared wavelengths where the mean free path length for mobile electrons is ~ 10 nm for most metals [30]. On the other hand, experimental results are always in semi-quantitative agreement with the classical model, which can be extended with more elaborate theory contingent on the initial agreement. Experiments at visible wavelengths have generally been more agreeable, but there is currently insufficient experimental data to form a complete survey. For this reason we find great value in reporting only the classical solutions, which, for this highly practical geometry, provides a new opportunity for experimental comparisons.

3. Model geometry

In this section we describe the geometry of our model, illustrated in Fig. 1(a). The model is rotationally symmetric, with the metal tip and point-like electric dipole \mathbf{p} positioned on the rotational axis. The dipole is oriented parallel to this axis and is placed 2nm above a glass substrate (refractive index of 1.5). The apex of the conical metal tip, which has been rounded to a sphere of radius = 10nm, is positioned at a variable distance D from the dipole. The cone radius at the top of the tip is $R_o = 3\mu\text{m}$ and the half-angle of the taper is 25 degrees (length of $6.43\mu\text{m}$). The shape of the metal tip is kept constant throughout this paper. A Perfectly Matched Layer (PML) of thickness equal to the free-space wavelength λ surrounds the region

of interest to ensure negligible back-reflections from impinging radiation. The PML at the top of the computational domain was tested to ensure that there is also negligible back-reflection from SPPs on the tip. In this way, an infinitely long tip is simulated, and we know that SPPs leaving our computational domain are only nonradiative (refer to Appendix A). The PML on the right starts at a distance of $3t_{\text{medium}}$ away from the top of the tip, where t_{medium} is the $1/e$ evanescent tail length of the SPP mode on the tip (defined in appendix A).

We sought only a Transverse Magnetic (TM) solution, which is sufficient for the present problem. The magnetic field, having only an azimuthal component (H_ϕ), was solved and subsequently used to calculate the only two electric field components (radial E_r and axial E_z). Post-processing of the solution, as described in Sections 2 and 5, provides the desired rates.

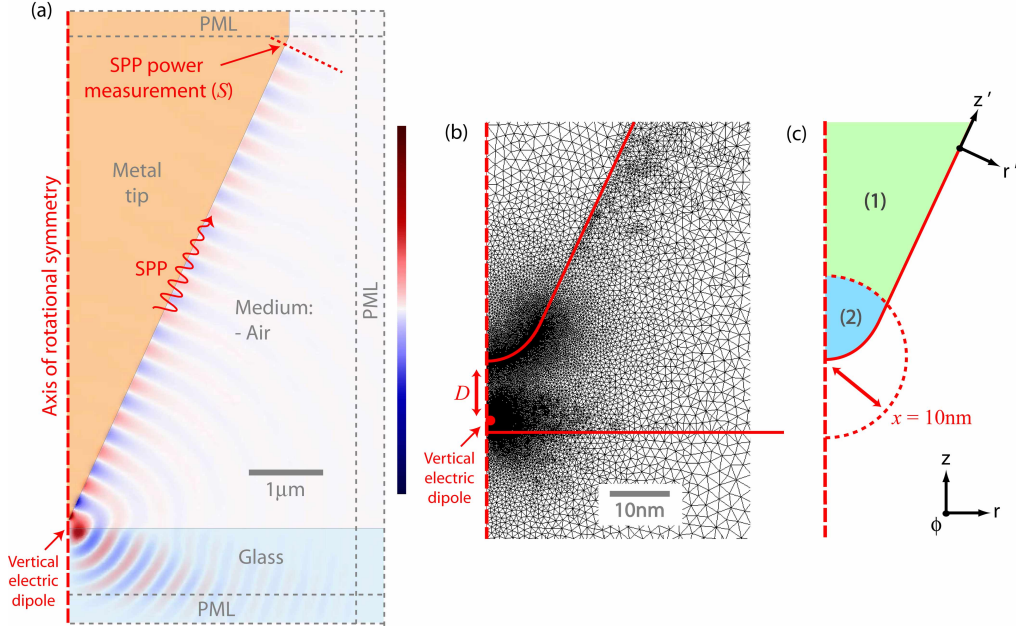


Fig. 1. (a) Example solution, $\text{Re}(H_\phi)$, with diagram overlay of the model geometry. This cross-section view is symmetric about indicated axis of rotation. In this figure, the tip (silver) is at a distance $D=100\text{nm}$ from the dipole and $\lambda=550\text{nm}$. The metal tip supports a propagating SPP that is clearly visible. The power in propagating SPPs remaining at the top of the tip is measured prior to the top PML, and is counted as nonradiative. (b) Example FEM meshing near the tip showing adaptive meshing and fine mesh near nano-scale features: $D=10\text{nm}$. (c) Diagram illustrating different parts of the tip where the integrated resistive losses are attributed to SPP losses (volume 1) and local energy transfer (volume 2).

4. Details of the finite element method (FEM)

We use a FEM to numerically solve Maxwell's equations in the frequency domain. Experimentally measured dielectric constants are used for metals at visible wavelengths, which can be found in published literature [31, 32]. The numerical model was defined, solved and analyzed in MATLAB employing the scripting functions 'COMSOL Multiphysics' (v3.3b with RF module). Adaptive meshing and re-meshing was essential to ensure accuracy in the solution involving vastly differing length scales, given the available computer memory. Initial meshing was coarse and inhomogeneous to resolve fine features in the model geometry and to give an approximate first solution. The final meshing was achieved through 2 iterations of re-solving with a finer triangulation that adapted to the previous solution. Convergence of the solution with mesh refinement shows that the rates presented are accurate to better than 3%. A typical mesh for the tip and dipole is shown in Fig. 1(b). The mesh is everywhere much finer than the free space wavelength and the final meshes typically resulted

in $O(10^6)$ degrees of freedom. The triangulation near the dipole can be as small as 10^{-15} m to capture rapidly varying features in the near-field.

The dipole is implemented as a small loop of fictitious magnetic current I_m , the equivalence of which can be straightforwardly derived from Maxwell's equations. Radii of $R_m \leq 2 \times 10^{-2}$ nm were chosen, which relates to the electric dipole moment by $|\mathbf{p}| = I_m \epsilon_0 \epsilon_{\text{medium}} \pi R_m^2$. Note that \mathbf{p} is independent of the tip and substrate.

The correctness and accuracy of our numerical model has been rigorously tested, including a comparison with the analytic solution for decay rates above a flat metallic surface.

5. Results: Empirical validation of the model

Having already introduced some background theory, we will now define and validate some novel terms that will be frequently used (also be found in Appendix B).

5.1. Partitioning of the tip

Separation of the total nonradiative rate into the contributions of γ_{SPP} and γ_{LET} (see Eq.3) is done in a simplified but effective manner, by separately integrating the resistive losses in two different parts of the tip. As is illustrated in Fig. 1(c), the tip is partitioned by a sphere of radius x , centered at the apex of the tip. We propose that x should be larger than the characteristic length for LET, and less than the characteristic length associated with a propagating SPP near the tip apex:

$$x_{\text{LET}} < x < x_{\text{SPP}}. \quad (5)$$

Prior literature frequently reports that very efficient (nonradiative) energy transfer from a molecule to a *flat* metallic surface occurs for separations of $< \sim 5$ nm. It is understood that the near-field of the molecule penetrates the metal and excites electron-hole pairs (excitons) that quench fluorescence [2, 3]. Classically, the process is described by induced charge-density oscillations (also called 'lossy surface waves'), which can be interpreted as dipole-dipole energy transfer (analogous to FRET) to a volume of dipoles below the surface. For a flat interface, the resulting distance dependence for the energy transfer rate γ_{LET} is [2]

$$\gamma_{\text{LET}} \approx \tilde{\gamma}_0 \frac{3}{8} \frac{1}{\epsilon_{\text{medium}}} \text{Im} \left\{ \frac{\epsilon_{\text{metal}} - \epsilon_{\text{medium}}}{\epsilon_{\text{metal}} + \epsilon_{\text{medium}}} \right\} \frac{c^3}{\omega^3} \frac{1}{D^3}, \quad (6)$$

where $\tilde{\gamma}_0 = \omega^3 \epsilon_{\text{medium}}^{-1/2} |\mathbf{p}|^2 / (12 \pi \epsilon_0 \hbar c^3)$ is the radiative decay rate of an isolated molecule (no substrate).

Equation 6 is derived by neglecting retardation effects (i.e. in the electrostatic limit). Thereby the contribution of propagating SPPs to this loss is excluded, leaving a purely *local* loss mechanism. By choosing the condition $\gamma_{\text{LET}} / \tilde{\gamma}_0 \gg 1$, we get $D \ll \sim 15$ nm for typical dielectric constants, suggesting that $x_{\text{LET}} \sim 7$ nm is a reasonable choice for our LET characteristic length scale.

For the characteristic SPP length scale we have used $x_{\text{SPP}} \sim 1/\text{Re}(k'_{\text{SPP}})$, where k'_{SPP} is the hypothetical SPP wave-vector near the tip apex. It is obtained by finding the analytic solution of the propagating TM SPP mode on a cylindrical metal wire of radius 10 nm [28, 33]. This length is significantly shorter than that of a SPP on a flat interface and was found to be in the range between 16 nm and 50 nm for a variety of metals and wavelengths.

Subsequent to the above considerations, we have chosen $x = 10$ nm to be constant for all simulations. We have found that the outcome is changed negligibly by varying the value of x up to 20 nm, and in some cases up to 40 nm.

5.2. Local energy-transfer (LET) rate: γ_{LET}

Our relation for calculating the LET rate is $\gamma_{\text{LET}} = P_{(2)} / (\hbar \omega)$, where $P_{(2)}$ is the power thermally dissipated within 10 nm of the tip apex (integrated over volume 2):

$$P_{(2)} = \frac{1}{2} \int_{(2)} \text{Re}(\mathbf{j}^* \cdot \mathbf{E}) dV. \quad (7)$$

The example shown in Fig. 2 compares a numerical solution with Eq.6. The agreement is excellent for $D < \sim 10\text{nm}$, above which retardation effects become important and the geometry of the tip becomes noticeably different to a flat interface. It clearly demonstrates that our simple procedure, based on a heuristically determined value for x , correctly separates the LET rate from the total nonradiative rate.

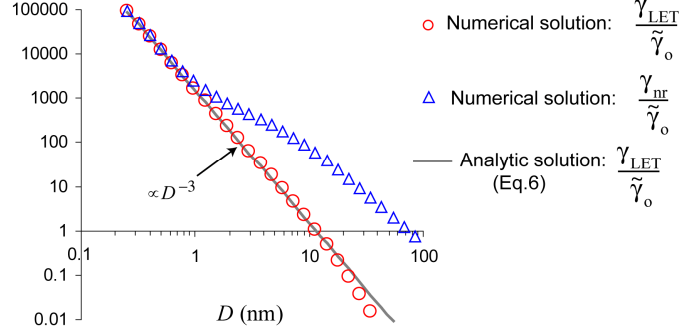


Fig. 2. Comparison of the numerical solution of $\gamma_{\text{LET}}/\tilde{\gamma}_0$ with the analytic solution (Eq.6) that neglects retardation effects. The numerical solution is for a silver tip using the geometry of Fig. 1(a) (without glass substrate) and $\lambda=550\text{nm}$. The analytic solution assumes the molecule is at distance D from a flat silver substrate (no tip). For comparison, the normalized total nonradiative rate $\gamma_{\text{nr}}/\tilde{\gamma}_0$ is shown.

5.3. Nonradiative surface plasmon polariton rate: γ_{SPP}

Our metal tip is capable of supporting propagating and localized SPPs. Due to symmetry, only transverse magnetic SPP can be excited, and then only efficiently when the tip enters the near-field of the molecule. It is important to emphasize that in lossy (realistic) metals, these SPP are always damped, with a probability of being either radiative or nonradiative (thermal). Since we are interested in simulating an infinitely long tip, and our computational domain is only finite, we cannot simply apply Eq.2. Our procedure for calculating the nonradiative-SPP rate is detailed in Appendix A. In summary, it is the sum of two contributions:

$$\gamma_{\text{SPP}} = \gamma_{(1)} + \gamma_{\text{prop}}$$

$\gamma_{(1)}$ is the rate at which SPPs are thermally dissipated into volume 1 of our finite tip and is simply calculated by integrating the resistive losses in this volume. γ_{prop} is related to the power remaining in propagating SPPs at the top of the metal tip, which is unambiguously calculated using modal methods. These SPPs are absorbed by the top PML in our computational domain, but would otherwise be thermally dissipated in an infinite tip, as discussed in Appendix A.

Using an example simulation with a silver tip, Fig. 3 highlights a number of very important characteristics. We emphasize that these characteristics are common for all cases presented in this paper.

Firstly, we demonstrate in Fig. 3(b) that $\gamma_{\text{prop}}/\gamma_{\text{SPP}} \cong \text{constant}$ for the full range of distances considered, particularly when $D < \sim 20\text{nm}$. This empirically validates our interpretation of γ_{SPP} as the nonradiative-SPP rate. Since $\gamma_{\text{SPP}}/\gamma_{\text{nr}}$ reduces sharply when $D < \sim 5\text{nm}$, we have additionally shown that our partitioning of tip into two parts based on x , meaningfully separates the SPP losses from all others. The analysis of Section 5.2 shows that the remaining losses are associated with LET, as proposed in Eq.3. The increase in $\gamma_{\text{prop}}/\gamma_{\text{SPP}}$ as the tip is retracted is not a numerical error. Since the SPPs on the tip have a probability of radiating, it is reasonable to assume that these SPPs can weakly couple from the far-field of the molecule. Therefore, launching of SPPs higher on the tip by radiation from the molecule can account for this behavior.

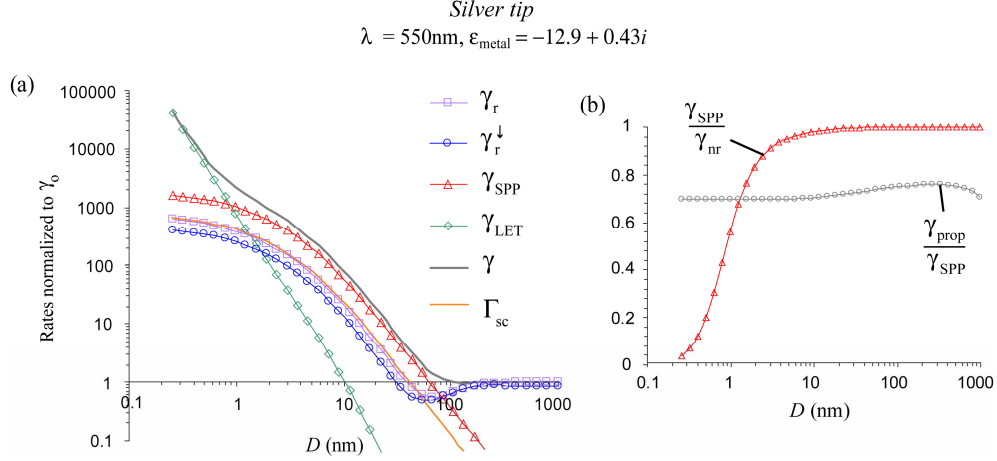


Fig. 3. Numerical solution for a silver tip using the geometry of Fig. 1(a). (a) All calculated rates shown. χ_{LET} approximates well Eq.6 when $D < \sim 10\text{nm}$. Γ_{sc} is defined in Section 6. (b) Validation of the tip partitioning: $\gamma_{\text{prop}}/\gamma_{\text{SPP}} \equiv \text{constant}$ when $D < \sim 20\text{nm}$ and $\gamma_{\text{SPP}}/\gamma_{\text{nr}} \neq \text{constant}$.

6. Relationship between the nonradiative-SPP and radiative decay rates

In Fig. 3(a), the correlation between the nonradiative-SPP and radiative decay rates for $D < 40\text{nm}$ is very clear. In Fig. 4 we see that χ is proportional to γ_{SPP} when $D < 40\text{nm}$. The proportionality is very accurately preserved although the rates individually increase by 3 orders of magnitude. This proportionality is characteristic of a coupling between the charge-density oscillations relating to SPPs on the tip and far-field radiation. We shall refer to the resulting proportionality simply as radiative-damping of SPPs. It is non-trivial to evaluate the details of this process and identify the locations on the tip where the SPPs are radiating. It is likely to be a distributed radiation from the tip apex and nearby. Additional scattering by the tip cannot be completely excluded as contributing to a change in the radiative rate. Further insight is provided in the following analysis.

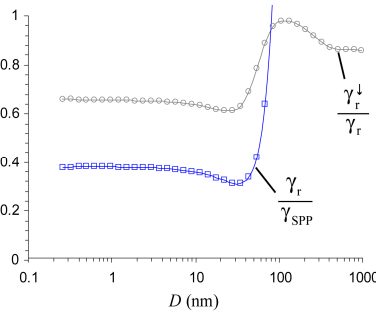


Fig. 4. Relationship between the radiative rate and the nonradiative-SPP rate. A change in the emission spatial distribution is observed.

We make a common decomposition of the total fields: $\mathbf{E} = \mathbf{E}_o + \mathbf{E}_s$, where \mathbf{E}_o is the solution for a molecule above the substrate (without tip) and \mathbf{E}_s is the light scattered by the tip. Equivalently, \mathbf{E}_s can be considered the radiation from the tip which is ‘sourced’ by the currents $\mathbf{j} = i\omega(\epsilon_{\text{metal}} - \epsilon_{\text{medium}})\epsilon_0\mathbf{E}$ induced within the tip by the molecule’s electric field. The rate of radiation scattered from the *entire* tip is therefore obtained by integrating the related Poynting vector over a surface enclosing the finite tip and subtracting the rate of propagating SPP leaving the top of the tip

$$\Gamma_{\text{sc}} = \frac{1}{2\hbar\omega} \int_{\text{tip}} \text{Re}(\mathbf{E}_s \times \mathbf{H}_s^*) \cdot \hat{\mathbf{n}} dS - \gamma_{\text{prop}}. \quad (8)$$

Γ_{sc} is plot in Fig. 3(a) for comparison with the other rates. There is good agreement with the radiative decay rate for $D < \sim 40\text{nm}$, confirming that the far-field photons at such distances are due to emission scattered by tip. In this regime $\gamma_r \approx \Gamma_{sc} \propto \gamma_{SPP}$, consistent with our model of radiative-damping among SPPs. However, Γ_{sc} is not strictly proportional to γ_{SPP} over the entire range of D . In the case of silver, this is only noticeable when $D > \sim 80\text{nm}$, but is more prominent for other dielectric constants. These accurate results are expected to represent a real physical process that becomes most visible when SPP radiative-damping is weak. The additional scattering may be consistent with an image-dipole model, as discussed in prior literature. The interpretation of this process is open for further investigation.

Within a linear approximation, we propose the probability of SPP radiative-damping σ can then be inferred from the nonradiative-SPP and radiative rates when the tip is near contact ($D \ll 10\text{nm}$). We define this probability as

$$\sigma_{(D \ll 10\text{nm})} = \frac{\gamma_r}{\gamma_{SPP} + \gamma_r}. \quad (9)$$

Using Eq.9 we can obtain the (linearised) total SPP rate by adding the radiative and nonradiative components: $\Gamma_{SPP} = \gamma_{SPP}/(1-\sigma)$.

It is also shown in Fig. 4 that the onset of the proportionality is simultaneous with a change in the spatial distribution of radiation. It is noteworthy for experimental considerations that the change in $\gamma_r^\downarrow/\gamma_r$ is minor.

7. Results: Exploratory simulations

The results presented in this section use the geometry shown in Fig. 1(a). Only the initial quantum efficiency, the metal (ϵ_{metal}) and wavelength are varied.

7.1. Influence of initial quantum efficiency – example with silver

Fig. 5 shows a comparison of two molecules of very different initial quantum efficiency. For $D < 10\text{nm}$ the similarity in the efficiencies is clear. This useful trend is obvious from Eq.4: when $\gamma_r + \gamma_{nr} \gg (1/q_0 - 1)\gamma_0$ (i.e. $\gamma_r + \gamma_{nr} \gg \gamma_0$) the apparent quantum efficiency of any molecule approximates the apparent quantum efficiency of a molecule with no intrinsic energy dissipation. The same is true for all other efficiencies. The significance is that this condition is easily satisfied in the system considered here and is one means by which the apparent brightness of fluorescence can be enhanced close to a metal tip.

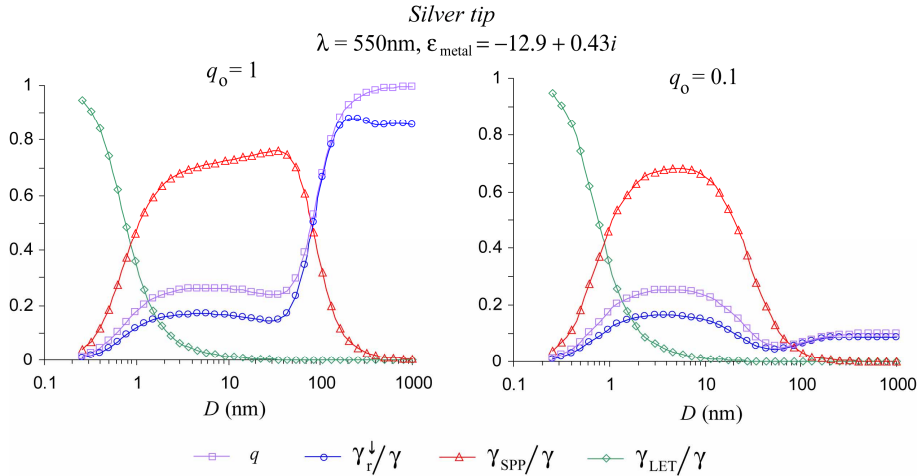


Fig. 5. Comparison of efficiencies for two different initial quantum efficiencies. The curves are nearly identical for $D < \sim 10\text{nm}$ (see text).

7.2. Losses

It is interesting to repeat the above calculation with the simple alteration of eliminating losses in the metal, setting $\text{Im}(\epsilon_{\text{metal}}) = 0$. The result is shown in Fig. 6. Here $\gamma_{\text{SPP}} \equiv \gamma_{\text{prop}}$ as there are no other losses. Since $\text{Re}(\epsilon_{\text{metal}}) \gg \text{Im}(\epsilon_{\text{metal}})$ we can expect the nonradiative-SPP rate to be weakly affected by the change, which is indeed demonstrated. Quenching by local energy transfer is completely eliminated, providing non-zero quantum efficiency for arbitrary separations.

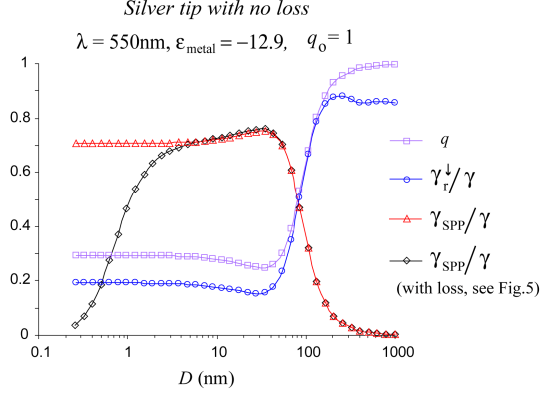


Fig. 6. A hypothetical silver tip without loss

7.3. Comparison with aluminum and gold

Comparative simulations for aluminum and gold tips are shown in Fig. 7. The emission wavelength remains 550nm to explore the influence of substantially different metal dielectric constants. The same characteristics are found universally. Quantitatively, the rates and efficiencies are different however, providing a useful reference. It is important to note that γ_{LET} approximates well Eq.6 when $D < \sim 10\text{nm}$ for both metals, despite being a higher rate than in the case of silver. We find again that SPP radiative-damping is the dominant contribution to the radiative decay rate for $D < \sim 40\text{nm}$. The probabilities for radiative-damping are $\sigma = 27\%$, $\sigma = 45\%$ and $\sigma = 4.1\%$ for silver, aluminum and gold respectively at $\lambda = 550\text{nm}$. The rate increases are enormous for all three metals.

Gold in particular shows a pronounced dip in the radiative rate around $D = 30\text{nm}$. A radiative rate reduction was observed in experiments with gold nano-particles, which is attributed to phase induced suppression of the radiative decay rate [34]. In our simulations the radiative rate reduction is coincident with the rise of the nonradiative-SPP rate, γ_{SPP} . The reduction is most visible in the case of gold due to the low probability of radiative-damping, σ . However, we note that a rate of radiative-damping linearly proportional to γ_{SPP} is not large enough at $D = 30\text{nm}$ to cause the radiative rate suppression by out-of-phase interference. At this dip the linearised SPP radiative-damping rate $\sigma \Gamma_{\text{SPP}}/\gamma_0$ is ~ 0.3 while $\Gamma_{\text{sc}}/\gamma_0$ is ~ 1 . As discussed in section 6, the physical interpretation of additional scattering from the tip is open for future study. It is worthwhile to highlight that the partial LDOS (or total decay rate) actually increases, despite the substantial radiative rate reduction. For a gold tip surrounded by water we have found γ/γ_0 to dip below 0.05. However, we have never observed the total rate γ reduced by a significant amount.

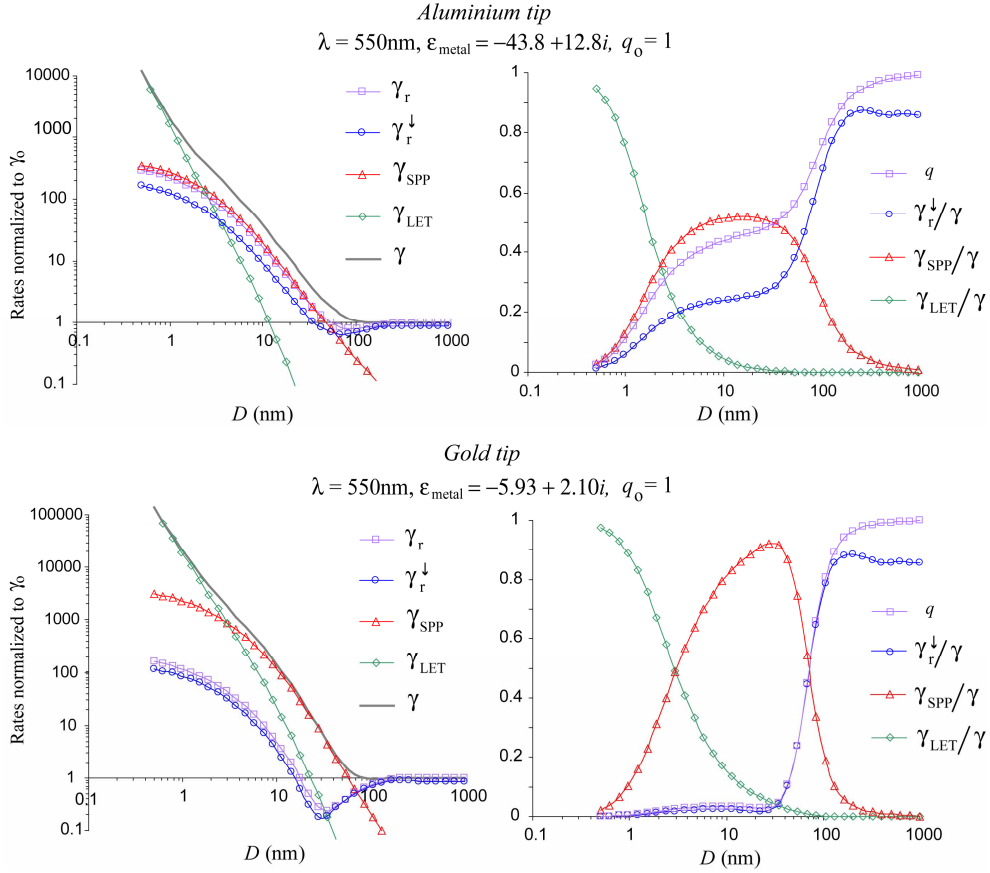


Fig. 7. Simulations for exploring the influence of metal dielectric constant. χ_{LET} approximates well Eq.6 when $D < \sim 10\text{nm}$ for both metals.

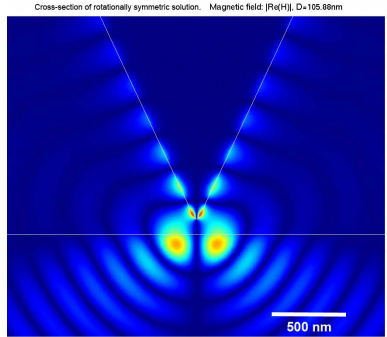


Fig. 8. Animation showing the approach of a gold tip ($\lambda = 565\text{nm}$). $|\text{Re}(H)|$ is plotted, which has been normalized at each frame (excitation is distance independent). The value of D is stated above. The prevalence of the radiative, SPP and LET rates at different distances is distinct. File size: 3.7 Mb.

7.4. Spectra with a gold tip

The electromagnetic response of gold at visible frequencies is known to exhibit a variety of useful properties. For this reason we show in Fig. 9 spectra for a gold tip at a fixed distance of 30nm. The figure demonstrates that a metal tip can significantly alter the observed spectral emission of a molecule. This distance was chosen where the peak in SPP efficiency occurs in

Fig. 6. Interestingly, we find peaks in the spectra at wavelengths of 560nm and 630nm for air and water respectively. Around these wavelengths the efficiency of creating SPPs is close to 100%. The origin of these peaks is not fully explained, as we will see from the following comparison. A planar interface between gold and one of these dielectrics permits a SPP resonance when $\text{Re}(\epsilon_{\text{metal}}) = -\epsilon_{\text{medium}}$. A thin metal rod has an identical resonance condition, as does Eq.6. Considering the possible dielectrics of air, water and glass (because of the substrate), a resonance at wavelengths longer than 520nm does not occur. For a sub-wavelength gold sphere, the plasmon resonance occurs where $\text{Re}(\epsilon_{\text{metal}}) = -2\epsilon_{\text{medium}}$. In this case, no resonances at wavelengths longer than 540nm occur. Neither of these phenomena explain the observed peaks nor the size of the shift with different surrounding media. A reverse process of nanofocusing, as studied in [28], also does not exhibit matching peaks.

Detailed analysis of the rates (not presented) shows that to the right of the peaks $\Gamma_{\text{SPP}}/\gamma \cong 1$, but σ increases rapidly to 0.7 and 0.56 in the case of air and water. To the left of the peak, $\Gamma_{\text{SPP}}/\gamma \sim 0.6$ and $\sigma < 0.05$ in both cases. This indicates an explanation related to a trade-off between a high probability of SPP radiative-damping at longer wavelengths, and inefficient SPP launching at shorter wavelengths due to a lack of high spatial-frequencies at $D=30\text{nm}$.

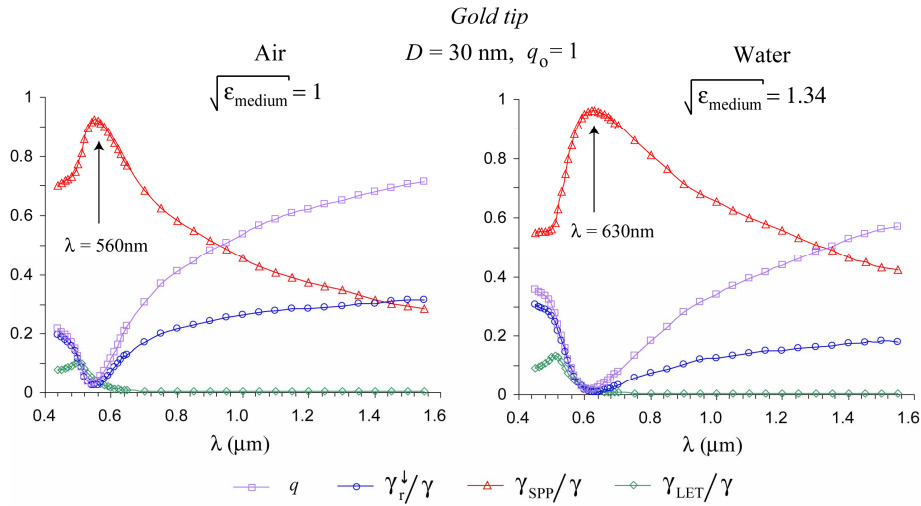


Fig. 9. Spectra for gold tips in air and water surrounding medium, with fixed $D=30\text{nm}$.

8. Discussion

The novel method of tip partitioning to calculate LET and nonradiative-SPP rates was proposed and validated empirically. With the above selection of results and numerous additional simulations not presented here, we have found the validation to be highly consistent for a variety of metals and wavelengths spanning the visible and near-infrared. We are therefore confident to state that the method is highly successful at quantifying SPP and LET rates in this geometry. We believe the method can be applied to many other problems involving fluorescence near metal particles and extended structures. A comparison with results for a flat interface [2, 3], where LET and SPP contributions are determined in the spatial-frequency domain, shows some similarity in the overall trends. An analogous spatial-frequency method may be possible for this geometry and others.

The nonradiative-SPP rate (and radiative rate when $D < 40\text{nm}$) was often found to be well fitted by an expression with $(D+D_0)^{-a}$, where a varied around the value 2 and D_0 ranged between 1nm and 10nm. The origin of this trend is presently unclear, but may lend itself to analytic study in the future. We note that the distance dependencies are distinctly different to those for nano-particles in the dipole limit [35], further advocating our full numerical study.

The scope of this paper has been limited to molecules with emission dipoles oriented parallel to the tip axis. This alone has provided a rich variety of physical phenomena. We

expect that perpendicularly oriented dipoles will give only a quantitatively different behavior for the nonradiative-SPP rate. So too will be off-axis alignment of the dipole and tip, as experienced in scanning probe microscopy. An extension of the present work to simulate both these effects is computationally intensive, but straightforward. The goal of the present work has been to introduce the method, and elucidate the basic physical processes observed. Future work can also include the evaluation of shifts in emission frequency expected for molecules near interfaces. They have been neglected so far as they are generally very small relative to the emission frequency.

9. Conclusion

We have proposed, empirically validated and applied a simple and robust method for determining the SPP and LET rates for a molecule near to a metal tip. A number of universal physical processes are observed. At separations less than $\sim 5\text{nm}$, energy transfer to the tip apex (the lowest 10nm) quickly becomes the dominant decay mechanism, which is nonradiative and unavoidable for lossy metals. This process is found to be accurately predicted by an analytic expression for the decay rate, having D^{-3} dependence. When the apex is in the near-field of the molecule, decay via SPP creation can occur at rates 3 orders of magnitude higher than the natural decay rate. Under such circumstances the apparent quantum efficiency of the molecule becomes independent of the initial quantum efficiency. For separations ranging from $\sim 10\text{nm}$ to $\sim 100\text{nm}$, the efficiency of (thermally dissipated) SPP creation has been sometimes observed to reach near 100%. A correlation between the SPP and radiative rates in this range suggests that, in general, the SPP decay channel is both radiative and nonradiative. We argue that the radiative-damping of SPPs accounts for the dramatic radiative rate enhancement at these separations and therefore determines the spatial distribution. The results presented can be directly applied to the design of scanning probe microscopes and interpretation of images.

Acknowledgments

We are thankful to R. Hillenbrand and F. Keilmann for helpful recommendations during the development of this paper. This work was supported by BMBF project 0312023C.

Appendix A: Calculation of γ_{SPP}

We are able to directly calculate the *nonradiative-SPP* rate γ_{SPP} from our numerical solution by summing two contributions: $\gamma_{\text{SPP}} = (P_{(1)} + P_{\text{prop}})/(\hbar\omega)$. The first term is the SPP power which is thermally dissipated in the *finite* tip

$$P_{(1)} = \frac{1}{2} \int_{(1)} \text{Re}(\mathbf{j}^* \cdot \mathbf{E}) dV, \quad (10)$$

where the volume of integration is indicated in Fig. 1(c), excluding the PML.

The second term is the power in propagating SPPs reaching the top of the metal tip, which will be fully absorbed in the top PML. This power would be thermally dissipated in the tip if it was infinite and should therefore be considered nonradiative. This is justified since any propagating SPP near the top of the tip closely approximates that of an SPP mode on a flat interface, where the radius is substantially larger than the wavelength ($R_0 \gg \lambda$) [33, 36]. It is well known that attenuation of such bound modes is purely absorptive and without radiation leakage.

P_{prop} is determined by first taking an inner-product [37] of the numerical solution with an analytic solution of the normalized SPP mode $\bar{\mathbf{E}}$ to obtain the amplitude of the SPP mode:

$$a = \frac{1}{2} \int_S (\bar{\mathbf{E}} \times \mathbf{H}) \cdot \hat{\mathbf{z}}' dr', \quad (11)$$

where the line integral is performed over the line S indicated in Fig. 1(a) and the coordinates are defined in Fig. 1(b). For the $\bar{\mathbf{E}}$ we use, as an excellent approximation, the well known

analytic solution of a SPP mode on a flat metal/dielectric interface. The propagation constant is $k_{\text{SPP}} = k_o [\epsilon_{\text{metal}} \epsilon_{\text{medium}} / (\epsilon_{\text{metal}} + \epsilon_{\text{medium}})]^{1/2}$.

Using to the $1/e$ tail-length of the mode-fields in the medium t_{medium} , and the skin depth in the metal t_{metal} , where $t_X = (k_{\text{SPP}}^2 - \epsilon_X k_o^2)^{-1/2}$. S is chosen to extend a distance of $3t_{\text{medium}}$ into the medium and a distance of $3t_{\text{metal}}$ into the metal. We use the *unconjugated* form of the inner product, which ensures orthogonality of the mode $\bar{\mathbf{E}}$ to all other bound and radiation modes, for both absorbing and non-absorbing waveguides. Since orthogonality is also ensured for all backward traveling modes (including any small back-reflection of the SPP mode from the PML layer), we are able to uniquely determine the amplitude of the *forward-propagating* mode only. The final expression for the remaining propagating SPP power is

$$P_{\text{prop}} \approx 2\pi R_o |a|^2 \bar{P}$$

$$\bar{P} = \frac{1}{2} \int (\bar{\mathbf{E}} \times \bar{\mathbf{H}}^*) \cdot \hat{\mathbf{z}}' dr' \quad (12)$$

where \bar{P} is the power of the analytic mode, normalized with the unconjugated inner-product (Eq.11). Our implementation of the above method was checked by varying R_o in a trial simulation, thereby changing the contributions of $P_{(1)}$ and P_{prop} . The tests show that the method is accurate to better than 10%.

Appendix B: Table of terms

Symbol	Quantity
D	Molecule-tip separation
γ	Total decay rate: $\gamma_r + \gamma_{\text{nr}} + \gamma$
γ_o	Radiative decay rate with the tip absent ($D \rightarrow \infty$)
$\tilde{\gamma}_o$	Radiative decay rate of isolated molecule (no substrate): $\omega^3 \epsilon_{\text{medium}}^{-1/2} \mathbf{p} ^2 / (12\pi\epsilon_o \hbar c^3)$
γ_i	Intrinsic decay rate due to intra-molecular energy dissipation
γ_{nr}	Total nonradiative decay rate: $\gamma_{\text{SPP}} + \gamma_{\text{LET}}$
γ_r	Radiative decay rate
γ_r^\downarrow	Radiative decay rate directed in the lower half space
γ_{SPP}	Nonradiative-SPP rate: $\gamma_{(1)} + \gamma_{\text{prop}}$
$\gamma_{(1)}$	Rate at which SPPs are thermally dissipated into volume 1.
γ_{prop}	Rate of propagating SPPs reaching the top of the metal tip. This is nonradiative.
γ_{LET}	Local Energy Transfer rate. Nonradiative dissipation in the tip apex (volume 2)
q	Apparent quantum efficiency: γ_r / γ
q_o	Initial quantum efficiency: $\gamma_o / (\gamma_o + \gamma)$
σ	Probability of SPP radiative-damping: $\gamma_r / (\gamma_r + \gamma_{\text{SPP}})$ evaluated when $D \ll 10\text{nm}$
Γ_{SPP}	Total SPP rate (radiative and nonradiative): $\gamma_{\text{SPP}} / (1 - \sigma)$
Γ_{sc}	Rate of light scattering by the tip